PAPER

Check for updates

Efficient light-induced reactive oxygen species production from a far-red ER-targeting BODIPY dye†

Shawn Swavey, [ID] *[a] Arnaud Quentel, [ID] [b] Matthew Grzesiak, [ID] [a] Cate Hawkins[a] and Pierre-Alexandre Vidi[b]

Generation of reactive oxygen species (ROS) within the ER evokes stress leading to immunogenic cell death. A red light activated BODIPY dye capable of subcellular localization within the ER producing high quantum yields of ROS is reported. The ability of this dye to act as a photodynamic therapy (PDT) agent in breast cancer cells suggests promising organelle-targeted therapeutics.

1. Introduction

Photodynamic therapy (PDT) was first approved for the treatment of bladder cancer in Canada in 1993. PDT is a non-invasive treatment modality which utilizes molecular oxygen, a photosensitizer (PS), and light to generate deleterious reactive oxygen species (ROS) within a specific microenvironment.[1,2] The most common route to cellular damage for FDA approved PDT agents involves energy transfer from the excited PS to ground state oxygen to generate singlet oxygen, referred to as a Type II mechanism. In contrast, the Type I mechanism involves electron transfer in which the excited PS can act as a reducing agent generating superoxide, radicals or hydrogen peroxide. The Type I mechanism is less dependent on molecular oxygen making this route a more effective PDT application under hypoxic conditions.

The first photosensitizer, Photofrin®, is a hematoporphyrin, a mixture of nearly sixty compounds. Despite difficulties in synthetic reproduction, low molar absorptivity within the PDT window leading to the need for high concentrations, as well as prolonged light sensitivity, Photofrin® is still the most common photosensitizer used in PDT.[3,4] Foscan®, *meta*-tetrahydroxyphenylchlorin, is a second-generation photosensitizer approved in 2001.[5] Despite its considerably higher toxicity compared to Photofrin®, Foscan® is extensively used for the treatment of advanced head and neck cancers. Operating by a Type II mechanism, studies have concluded that Foscan® localizes within the endoplasmic reticulum (ER) initiating organelle photodamage and apoptotic events after irradiation.[6]

The ER is the organelle providing a milieu for assembling and folding of proteins, protein modification as well as protein secretion. A large organelle in the cell, making up over 10% of the cell's volume, the ER is composed of rough and smooth domains. Accumulation of unfolded or misfolded proteins results in ER stress, which can lead to a variety of health conditions including tumorigenesis, neurodegenerative diseases, and diabetes.[7–9] As such, the ER is an excellent molecular target for PDT. Excessive ER stress has been linked to immunogenic cancer cell death (ICD) resulting from damage associated molecular patterns (DAMPs).[10] ER stress can be triggered by excess ROS; however, given the short half-life of $^1O_2$ (<300 ns) this strategy for cancer therapy requires developing bimodal PS's capable of ER-localization along with light driven $^1O_2$ production.[11–15]

Boron dipyrromethene (4,4-difluoro-4-bora-3*a*,4*a*-diaza-*s*-indacene) or BODIPY represent a class of fluorophores marked by intense absorption and emission within the visible region of the electromagnetic spectrum with high quantum yields and intrinsic photostability. There are relatively few BODIPY dyes specifically designed to target the ER.[16–20] Their emissive properties and low cytotoxicity make them ideal as fluorescent probes for biological systems; however, post-functionalization is often required to ensure specific localization. For example, the commercial ER dyes ER-Tracker™ Green and ER-Tracker™ Red are covalently attached to glibenclamide; a drug used to treat hypoglycemia. These ER dyes require the glibenclamide for binding to sulfonylurea receptors expressed by ER.[21] Of course, the amount of ER labelling is dependent on the expression level of these receptors and binding to these receptors may interfere with normal ER function.

First generation BODIPY dyes, while excellent as fluorescent probes for cellular imaging, were not amenable as photosensitizers for phototherapeutic applications. This is due to their inability to access the triplet state preventing the formation of ROS. Population of the triplet excited state has been achieved by

aDepartment of Chemistry, University of Dayton, Dayton, OH 45469, USA. E-mail: sswavey1@udayton.edu; Web: https://www.udayton.edu/directory/artssciences/chemistry/swavey_shawn.php; Tel: +1-937-229-3145

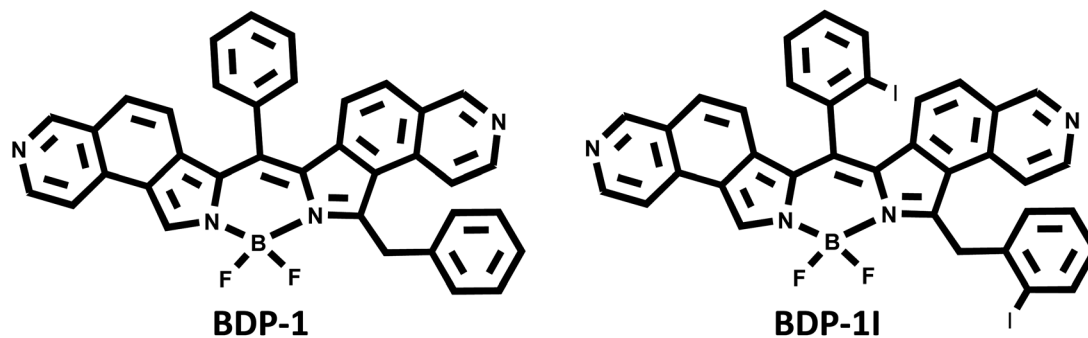*bLaboratoire InGenO, Institut de Cancérologie de l'Ouest, Angers, 49055, France*

Fig. 1 Structures of isoquinol-based BODIPY dyes BDP-1 and BDP-1I.

addition of heavy atoms such as bromine or iodine atoms into the BODIPY core[22–26] or through ancillary metal ion complexes.[27–30] This "heavy atom" effect results in enhanced spin orbit coupling increasing the population of the triplet excited state through intersystem crossing consequently leading to increased production of ROS. Although PDT is marketed as a more targeted therapy compared to most chemotherapeutics a concerted effort to develop PDT agents capable of localizing within specific organelles is of considerable interest. Recent advances in BODIPY photosensitizers have resulted in PDT agents capable of localizing within cellular organelles such as the mitochondria and the endoplasmic reticulum.[31,32]

Our laboratory has recently developed a BODIPY scaffold capable of absorption and emission in the far-red region of the electromagnetic spectrum and preliminary characterization suggests ER localization.[33] Utilizing isoquino[5,6-c]pyrrole along with readily available benzaldehyde, the π-extended dipyrrin can be synthesized under mild conditions without the need for oxidizing agents in under 3 min. Reaction with triethylamine and boron trifluoride etherate by standard procedures gives the fluorescent probe **BDP-1** (Fig. 1).[34]

Attempts of iodinating the core of **BDP-1** proved impossible; however, a recent study indicated that efficient intersystem crossing to the triplet state can be achieved by incorporating iodine within the *meso*-substituent of BODIPY's.[35] Since we have identified the BODIPY-scaffold leading to ER-localization, we were able to synthesize **BDP-1I** in good yield by replacing benzaldehyde with commercially available 2-iodobenzaldehyde (Fig. 1). This report describes the spectroscopic properties of **BDP-1I** and its ability to generate reactive oxygen species (ROS) when irradiated with low energy light. The ability of this new photosensitizer to localize within the ER of several cancer cell lines and ultimately cause cell death upon irradiation is presented.

2. Materials and methods

2.1. Materials

Reagents were purchased from Sigma Aldrich or Thermo Fisher. Solvents were reagent grade and used without further purification. Isoquino[5,6-c]pyrrole was synthesized as previously described.[36] **BDP-1** was synthesized as previously described.[33] Chromatography was performed on a Teledyne CombiflashRf+

equipped with UV detection. High-resolution mass spectroscopy was performed at the Mass Spectrometry and Proteomics facility at the Ohio State University. Elemental analysis was performed at Atlantic Microlabs, Norcross, GA. ^{1}H NMR were recorded on a Bruker 400 MHz NMR spectrophotomer at 298 K. Chemical shifts (δ) are given in ppm relative to CDCl$_3$ (7.26 ppm for ^{1}H).

2.2. Methods

2.2.1. Synthesis of BDP-1I. To a 50 mL round bottom flask 50.0 mg (0.30 mmol) of isoquino[5,6-c]pyrrole and 104 mg (0.45 mmol) of 2-iodobenzaldehyde were combined. Approximately 1 mL of a 1/1 methanol/dichloromethane solution was added to give a homogenous solution. To this solution was added 10 drops of trifluoroacetic acid. The solvent was then removed under reduced pressure at approximately 70 °C. The resulting paste was heated up to 80 °C at which point a purple paste formed. The round bottom flask was capped with a septum and purged with nitrogen followed by the addition of 4–6 mL of dry toluene and placed in an oil bath preset to 80 °C. Under a nitrogen purge approximately 150 μL of Et$_3$N followed by 200 μL of BF$_3$·OEt$_2$ was added and the resulting solution was allowed to stir for 20 min. After cooling to room temperature, the solution was taken up in DCM and chromatographed twice on silica with DCM and increasing amounts of ethyl acetate. The fluorescent red product was collected at 50/50 DCM/ethyl acetate. The product was recrystallized from an ethyl acetate/ hexanes mixture to give a deep blue powder (32 mg, 27%).

^{1}H NMR (400 MHz, CDCl$_3$) δ 9.12 (d, J = 18.1 Hz, 2H), 8.86 (s, 1H), 8.68 (s, 1H), 8.50 (s, 1H), 8.28 (d, J = 7.9 Hz, 1H), 8.02 (t, J = 7.8 Hz, 2H), 7.79 (t, J = 7.4 Hz, 1H), 7.68 (d, J = 7.3 Hz, 1H), 7.58 (dd, J = 18.9, 8.3 Hz, 4H), 7.11 (t, J = 7.5 Hz, 1H), 6.95 (t, J = 7.4 Hz, 1H), 6.82 (d, J = 7.6 Hz, 1H), 6.38 (d, J = 8.9 Hz, 1H), 6.29 (d, J = 8.9 Hz, 1H), 5.14 (s, 2H).

HR-ES-MS: m/z = 812.99781 [M + H]$^+$ (calcd for C$_{36}$H$_{22}$N$_4$BF$_2$I$_2$ 812.99951).

Elemental analysis. Anal. calc. for C$_{36}$H$_{21}$N$_4$BF$_2$I$_2$·H$_2$O: % C = 52.08, % H = 2.79, % N = 6.75; found: % C = 52.02, % H = 2.90, % N = 6.84.

2.2.2. Spectroscopy. Electronic absorption spectra were recorded at room temperature using an HP8453 photodiode array spectrophotometer with 2 nm resolution. All spectra were recorded at 298 K. Room temperature luminescence spectra in

a 1 cm quartz spectrophotometer fluorescence cell (Starna) in DCM were run on a Cary Eclipse fluorescence spectrophotometer. Quantum yields were determined at room temperature in HPLC grade DCM relative to Rhodamine-6G as the reference (φ = 0.94 in ethanol). The quantum yields were obtained using the following eqn (1):

$$\varphi_s = \varphi_r[A_r\eta_s^2 D_s/A_s\eta_r^2 D_r] \qquad (1)$$

where s and r indicating the sample and reference, respectively, A is the absorbance at the excitation wavelength, η is the average refractive index of the solution, and D is the integrated area under the emission spectrum.

2.2.3. DPBF studies. Acetonitrile solutions of 1,3-diphenylisobenzofuran (DPBF, ROS quencher) and **BDP-1I**, **BDP-1**, and RB at roughly a 30 to 1 ratio in quartz cuvettes were irradiated in the presence of oxygen using a 300 W mercury-arc lamp (equipped with a long band pass filter cutting off wavelengths below 550 nm). The progress of singlet oxygen production, monitored using the HP8453 photodiode array spectrometer, was determined by observing the decrease in the maximum absorption band at 411 nm associated with the singlet oxygen trap DPBF as a function of irradiation time. The slopes were calculated and compared with Rose Bengal (RB) as a reference (Φ_Δ = 0.76 in methanol). Singlet oxygen quantum yields were calculated according to eqn (2):[37,38]

$$\phi_\Delta (PS) = \phi_\Delta (R) \times m(PS)/m(R) \times F(R)/F(PS) \qquad (2)$$

where PS and R designate photosensitizer (**BDP-1I** or **BDP-1**) and reference dye (RB) respectively. m is the slope of difference in change in absorbance of DPBF at absorbance maxima with the irradiation time. F is the absorption correction factor, which is given as $F = 1 - 10^{-OD}$

2.2.4. ABDA studies. Acetonitrile solutions of 9,10-anthracenediyl-bis(methylene) dimalonic acid (ABDA, $^1O_2$ quencher) and RB, **BDP-1I**, and **BDP-1** in quartz cuvettes were irradiated in the presence of oxygen using a 300 W mercury-arc lamp (equipped with a long band pass filter cutting off wavelengths below 550 nm). The progress of singlet oxygen production, monitored using the HP8453 photodiode array spectrometer, was determined by observing the decrease in the maximum absorption bands associated with the singlet oxygen trap DPBF as a function of irradiation time. The slopes were calculated and compared with Rose Bengal (RB) as a reference (Φ_Δ = 0.76 in methanol). Singlet oxygen quantum yields were calculated according to eqn (3):[39]

$$\Phi_{probe} = \Phi_{RB} (K_{probe}A_{RB}/K_{RB}A_{pro}) \qquad (3)$$

where K_{probe} and K_{RB} were the decomposition rate constants of ABDA in the presence of the probe and RB, respectively. Φ_{RB} was the $^1O_2$ quantum yield of RB (Φ_{RB} = 0.76 in methanol). The natural logarithm of the absorbance ratio (A_0/A) of ABDA at 377 nm was plotted against irradiation time and the slope is regarded as the decomposition rate.

2.2.5. DHE studies. Acetonitrile solutions of dihydroethidium (DHE, superoxide quencher) and **BDP-1I** in fluorescence quartz cuvettes were irradiated with a 300 W mercury arc lamp equipped with a 550 nm long band-pass filter. The progress of superoxide production, monitored using a Cary Eclipse fluorometer, was determined by the increase of a broad emission spectrum upon excitation at 500 nm due to the production of ethidium bromide.

2.2.6. Cyclic voltammetry. Cyclic voltammograms were recorded under a nitrogen/air atmosphere using a one-compartment, three electrode cell, CH-Instruments, equipped with a platinum wire auxiliary electrode. The working electrode was a 2.0 mm diameter glassy carbon disk from CH-Instruments, which was polished first using 0.30 μm followed by 0.05 μm alumina polish (Buehler) and then sonicated for 10 s prior to use. Potentials were referenced to a Ag/AgCl aqueous electrode with ferrocene as an internal standard, CH-Instruments. The supporting electrolyte was 0.1 M tetrabutylammonium hexafluorophosphate (TBAP) and the measurements were made in dry acetonitrile.

2.3. Cell studies

2.3.1. Cell culture. Non-malignant HMT-3522 S1 breast epithelial cells (S1) were propagated in H14 medium (DMEM/F12) supplemented with 50 ng mL^{-1} recombinant human prolactin, 250 ng mL^{-1} human insulin, 1.4 mM hydrocortisone, 0.1 nM β-estradiol, 2.6 ng mL^{-1} sodium selenite, 10 mg mL^{-1} transferrin, and 5 ng mL^{-1} epidermal growth factor (EGF). HMT-3522 T4 breast cancer cells were cultured in H14 medium lacking EGF. MDA-MB-231 breast cancer cells were cultured in DMEM/F12 supplemented with 10% fetal bovine serum (FBS). Cells were kept in a humidified incubator at 37 °C, 5% CO$_2$. For microscopy, S1 cells were seeded at a density of 25 000 cells per cm^2 on glass-bottom 35 mm dishes (MatTek) and cultured for 10 days. MDA-MB-231 cells were seeded in the same dishes or in glass-bottom 96-well plates at a density of 44 000 cells per cm^2 and cultured for 2 days.

2.3.2. Cell staining. **BDP-1** and **BDP-1I** were diluted to 1 μM in phenol red-free culture medium and incubated with the cells for 15 min at 37 °C. For dose response analysis, a serial dilution was made in medium. ER-Tracker Green (2 μM; Invitrogen) was added for 30 min on cell cultures. MitoTracker Green (100 nM; Invitrogen) was incubated for 15 min with the cells. Cell nuclei were stained with Hoechst 33342. Cells were rinsed and imaged in phenol red-free culture medium.

2.3.3. Cell fixation and immunostaining. Samples were rinsed with PBS, fixed 20 min with 10% formalin, washed with PBS glycine (50 mM), permeabilized 10 min with 0.5% Triton X-100, and blocked with 10% goat serum in immunofluorescence buffer (IF; 130 mM NaCl, 13.2 mM Na$_2$HPO$_4$, 3.5 mM NaH$_2$PO$_4$, 0.1% bovine serum albumin, 0.05% NaN$_3$, 0.2% Triton X-100, and 0.05% Tween 20). Samples were incubated overnight at 4 °C with KDEL antibodies (1/200; AbCam cat# EPR12668) diluted in blocking buffer. After three washes with IF buffer, samples were incubated with AlexaFluor488-coupled secondary antibodies (1/500; Life Technologies) and washed again with IF. Nuclei were stained with 0.5 μg mL^{-1} 4′,6-diamidino-2-phenylindole (DAPI). Samples were mounted using ProLong Gold antifade (Molecular probes).
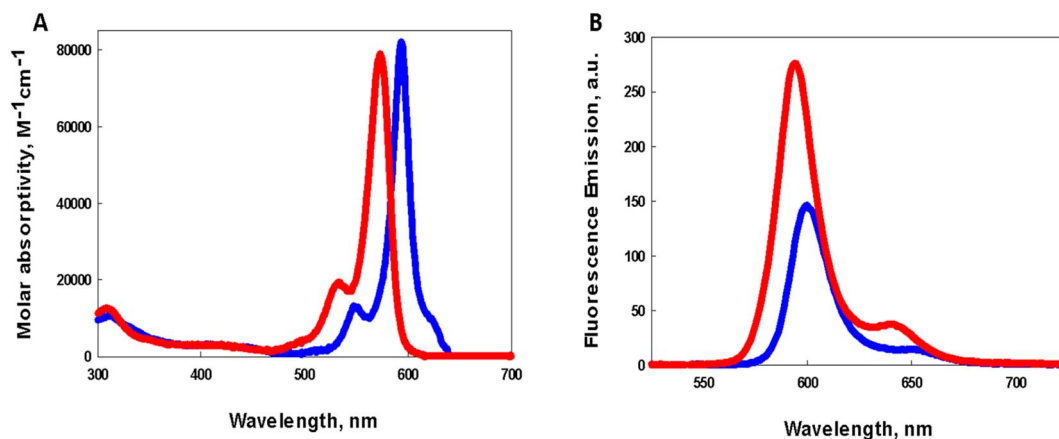
Fig. 2 (A) Absorption spectrum of dichloromethane solutions of **BDP-1** (red) and **BDP-1I** (blue) (B) emission spectra of dichloromethane solutions of **BDP-1** (red) and **BDP-1I** (blue) upon excitation at their respective absorption maxima.

2.3.4. Cell irradiation and viability assessment. Regions of the culture were illuminated at 40× magnification for 5 min using the X-Cite TURBO (Excelitas) light engine of the microscope (505–550 nm LED; 100% intensity) combined to a 'Cy3' excitation filter (554/23 nm). Alternatively, and to better match the illumination used for *in vitro* assays, emission filters were removed from the light source and two LEDs were used in combination (at 100% intensity) for illumination over the 555–610 and 615–660 nm wavelengths. Positions for illumination were marked with etched 'x' on the coverslip before cell culture. For experiments with cells in 96-well plates, the center positions of the wells were illuminated and saved. Cells were imaged and returned to the incubator for re-imaging 18 h or 40 h later to assess viability, based on morphology (bright field images), in irradiated and non-irradiated zones. Alternatively, cell viability was determined using the LIVE/DEAD viability assay kit (Invitrogen). This assay is based on live cell labeling with calcein AM (green fluorescence) and dead cell labeling with the deep red SYTOX dye. Cell nuclei were stained with Hoechst before imaging.

2.3.5. Microscopy. Cells were imaged with an inverted Olympus IX83 microscope, using a 40× air (N. A. = 0.95) or a 60× silicon oil immersion objective (N. A. = 1.30). Excitation light was filtered using a 'DAPI' (378/52 EX; 460/50 EM) filter set for Hoechst and DAPI, a 'FITC' (474/27 EX; 525/50 EM) filter set for AlexaFluor488, ER-Tracker Green, and MitoTracker Green, and a 'Cy3' (554/23 EX; 600/37 EM) filter set for **BDP-1** and **BDP-1I**. Fluorescent signals were captured with a qCMOS camera (Hamamatsu ORCA-Quest). Fluorescence intensity profiles were visualized in FIJI (**https://fiji.sc**). For live imaging, cells were kept at 37 °C with a stage-top incubator (TokaiHit). For assessment of LIVE/DEAD viability staining, images were taken with a 10× lens, using 'DAPI', 'FITC' and 'Cy5' (635/18 EX; 700/75 EM) filter sets. To calculate the proportion of live cells, cell nuclei (Hoechst signals) were segmented using StarDist (**https://github.com/stardist/stardist**) in FIJI. SYTOX DeepRed intensities were retrieved in the corresponding regions of interest and set as present/absent according to predetermined thresholds. The number of live cells in an image was calculated by subtracting the number of SYTOX-positive cells from the total cell number.

3. Results and discussion

3.1. Spectroscopy

Comparison of the photophysical properties of both photosensitizers in dichloromethane is illustrated in Fig. 2. **BDP-1** shows a sharp intense absorption with $\lambda_{max} = 585$ nm (Fig. 2A red) while the absorption peak for **BDP-1I** shows a modest bathochromic shift of 344 cm^{-1} to a $\lambda_{max} = 597$ nm (Fig. 2A, blue). Molar absorptivities of **BDP-1** (ref. 33) and **BDP-1I** at their peak absorptions were determined to be 79 000 M^{-1} cm^{-1} and 83 000 M^{-1} cm^{-1} (ESI Fig. S1†), respectively. Emission spectra resulting from excitation of dichloromethane solutions of **BDP-1** and **BDP-1I** at their absorption maxima is illustrated in Fig. 2B, with red and blue lines, respectively. Emission peaks at 595 nm (**BDP-1**) and 608 nm (**BDP-1I**) give rise to Stokes shifts of 287 cm^{-1} and 273 cm^{-1} respectively. Luminescence quantum yield of **BDP-1** (0.75) is considerably greater than that for **BDP-1I** (0.38) most likely due to the heavy atom effect allowing for **BDP-1I** to populate the triplet excited state through enhanced spin–orbit coupling leading to intersystem crossing.

3.2. ROS generation

The efficiency of ROS generation was monitored by electronic spectroscopy by observing the decay of the absorption band associated with the $^1O_2$ and $O_2^{\bullet-}$ scavenger (1,3-diphenylisobenzofuran, DPBF) upon irradiation with low energy light.[40] Acetonitrile solutions of DPBF and the photosensitizers Rose Bengal (RB), **BDP-1,** and **BDP-1I** with a 30-fold excess of scavenger were irradiated with a 100 W mercury-arc lamp equipped with a 550 nm long band-pass filter. Each irradiation experiment was run in triplicate (ESI, Fig. S2–S4†). Fig. 3A illustrates one of the trials with **BDP-1I** as the photosensitizer. Plots of the change in absorption (ΔAbs) of DPBF *versus* irradiation time with $^1O_2$ sensitizer RB (black line), **BDP-1I** (blue line), and **BDP-1**
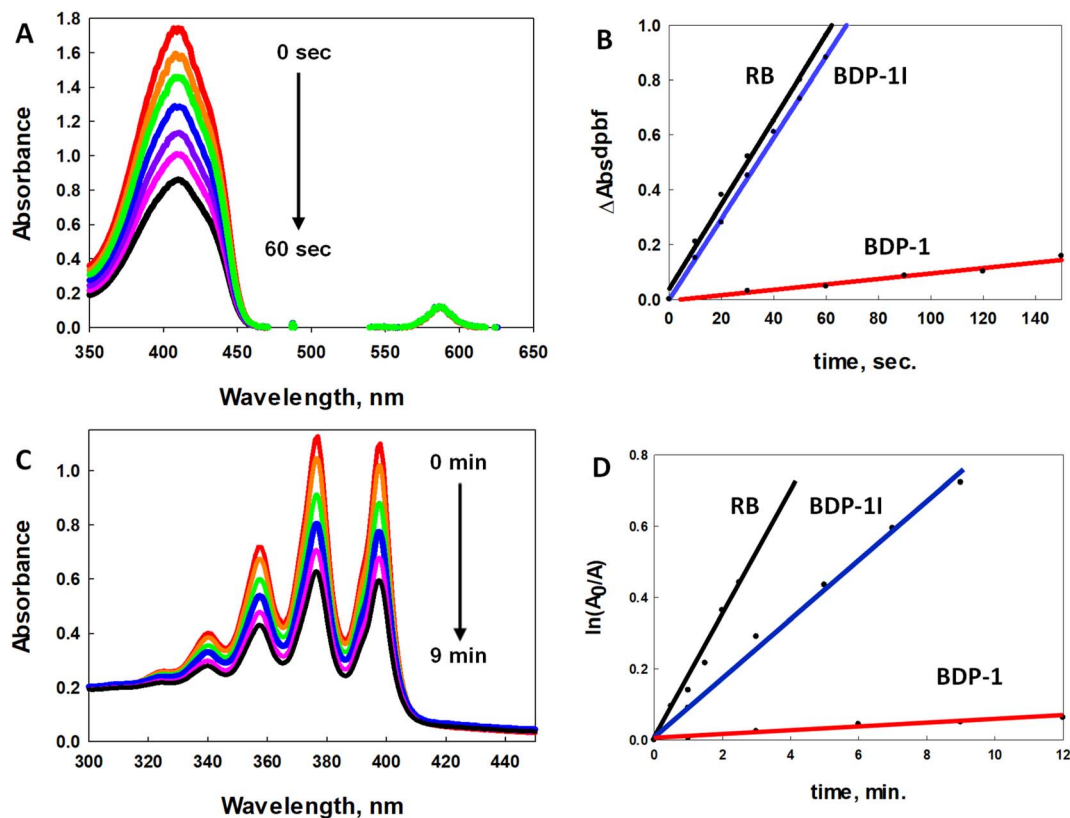
Fig. 3 (A) Electronic spectra of acetonitrile solution of the oxygen scavenger DPBF and **BDP-1I** after irradiation with 300 W lamp equipped with a 550 nm long band-pass filter. (B) Comparison of DPBF absorption differences *versus* irradiation time for Rose Bengal (RB, reference, black), **BDP-1I** (blue) and **BDP-1** (red). (C) Electronic spectra of acetonitrile solution of the singlet oxygen scavenger ABDA and **BDP-1I** irradiated with the same light source as (A). (D) Comparison of ABDA absorption differences *versus* irradiation time for RB (reference, black), **BDP-1I** (blue) and **BDP-1** (red).

(red line) fit to a linear regression are illustrated in Fig. 3B. **BDP-1I** shows excellent $^1O_2$ quantum yield (Φ_Δ) of 0.69($\pm$0.01) comparable to RB, Φ_Δ = 0.76 in methanol.[41] The non-iodinated **BDP-1** showed very little change in the absorption of the DPBF even with extended irradiation times resulting in a low $^1O_2$

quantum yield Φ_Δ = 0.063($\pm$0.07). This illustrates the role of the heavy atom effect despite not being attached directly to the BDP core.

While DPBF fluorescence quenching is typically associated with $^1O_2$ production (Type II) it is also quenched by $O_2^{\bullet-}$ (Type
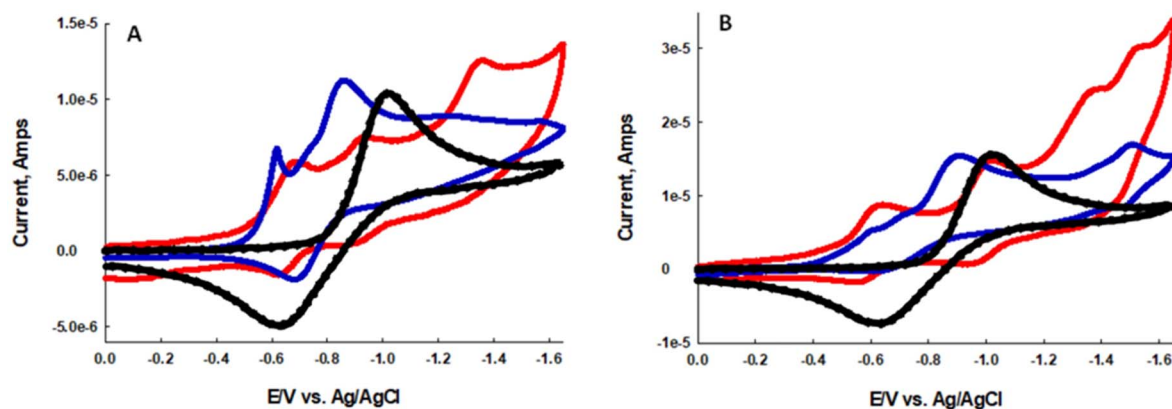

Fig. 4 (A) Cyclic voltammetry of an acetonitrile solution saturated with air (black dotted line), acetonitrile solution of 5 μM **BDP-1** in an air saturated solution (blue line), and in the absence of oxygen (red line). (B) Cyclic voltammetry of an acetonitrile solution saturated with air (black dotted line), acetonitrile solution of 5 μM **BDP-1I** in an air saturated solution (blue line), and in the absence of oxygen (red line). The supporting electrolyte was tetrabutyl ammonium hexafluorophosphate (TBAP), with a glassy carbon working electrode, platinum wire auxiliary, and Ag/AgCl reference electrode. Scan rates were 100 mV s^{-1}.

I); therefore, studies using more specific ROS quenchers were employed to better understand the mechanism of ROS production.[42] Specific detection of $^1O_2$ was achieved with the probe 9,10-anthracenediylbis(methylene)dimalonic acid (ABDA); however, longer irradiation times are needed with ABDA *versus* DPBF due to its much lower $^1O_2$ reactivity.[43] Fig. 3C illustrates the effect on the electronic absorption of ABDA as a function of irradiation of a solution of ABDA and **BDP-1I**. The natural logarithm of the absorbance ratio (A_0/A) of ABDA at 377 nm plotted *versus* irradiation time[44] with $^1O_2$ sensitizer RB (black line), **BDP-1I** (blue line), and **BDP-1** (red line) fit to

a linear regression are illustrated in Fig. 3D. All of the experiments were run in duplicate (ESI Fig. S5–S7†). The $^1O_2$ quantum yield (Φ_Δ) for **BDP-1I** and **BDP-1** were determined to be 0.38 and 0.03, respectively. Notably, the Φ_Δ for both BDP dyes were roughly half their values obtained from the DPBF study. To further assess ROS generation, studies using dihydroethidium (DHE), a $O_2^{\cdot-}$ scavenger, were performed. When solutions of DHE and PS are irradiated, $O_2^{\cdot-}$ produced by the PS oxidizes DHE to 2-hydroxy ethidium, generating a broad emission spectrum (590–630 nm) when excited at 500 nm.[45] Irradiated acetonitrile solutions of DHE/**BDP-1I** and DHE/**BDP-1** result in
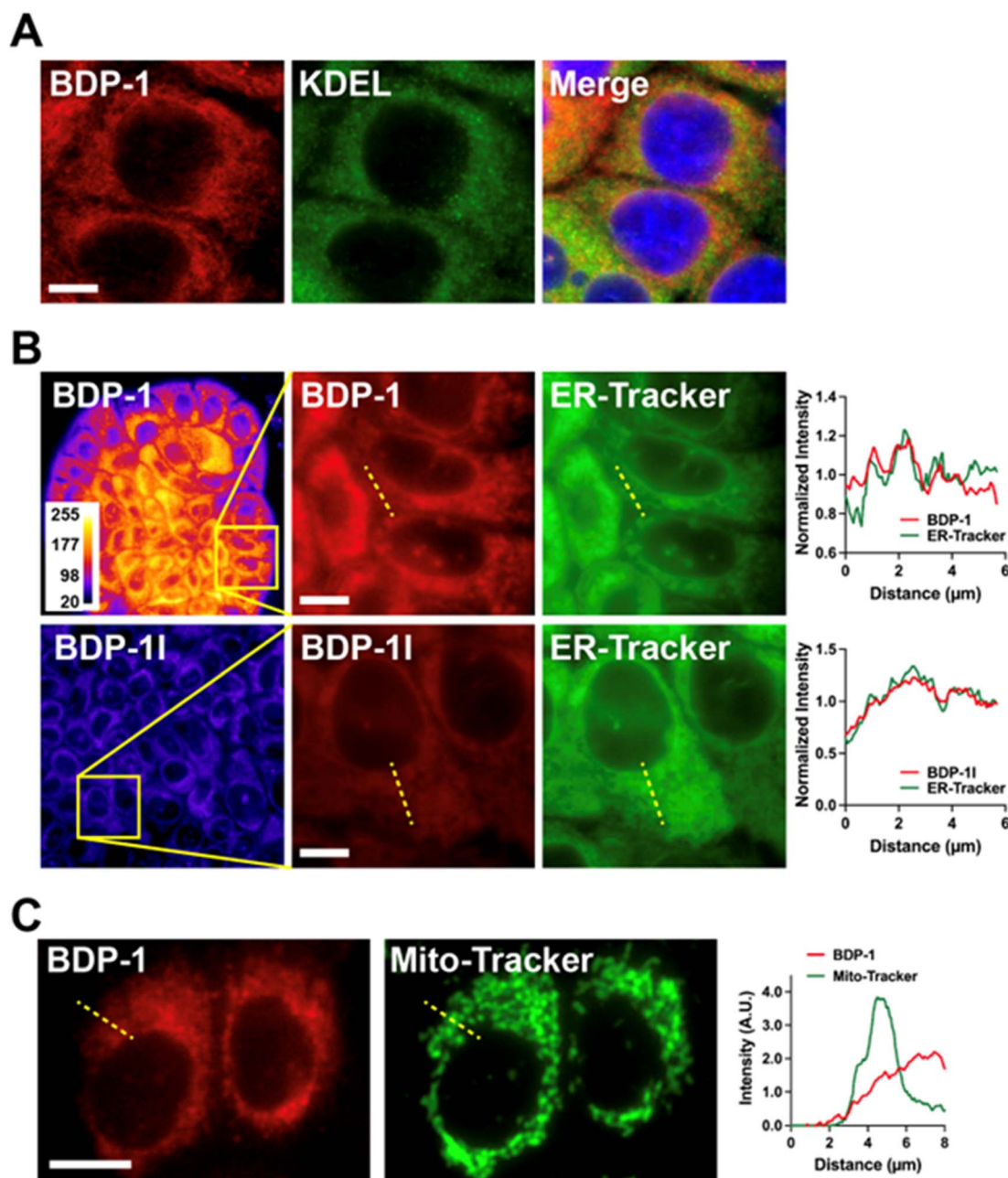

Fig. 5 Subcellular localization of **BDP-1** and **BDP-1I**. (A) Breast epithelial cells were stained with **BDP-1**, then fixed and immunostained for the KDEL peptide sequence. (B) Live cell images of cells co-stained with ER-Tracker and **BDP-1** or **BDP-1I**. Intensity profiles correspond to the dotted lines. Overview images (first column) are displayed as heatmaps to visualize fluorescence intensities. (C) Live cell images after co-staining cells with MitoTracker and **BDP-1**. Scale bars, 10 μm.

broadened emission spectra as a function of irradiation time (ESI Fig. S8 and S9†), indicating that both dyes produce $O_2^{\bullet-}$.

In an effort to better understand why **BDP-1I** and **BDP-1** produce $O_2^{\bullet-}$ by a Type I mechanism we evaluated the electrochemical properties of the dyes in the presence and absence of molecular oxygen. In oxygen saturated dry acetonitrile oxygen is known to undergo a quasi-reversible one-electron reduction to $O_2^{\bullet-}$. Overlapping reduction potentials of the dyes with the reduction potential of oxygen is an indicator of the ability to produce $O_2^{\bullet-}$ by a Type I mechanism.[46–49] Fig. 4A and B illustrate the CV's of **BDP-1** and **BDP-1I**, respectively, in dry acetonitrile in the presence and absence of oxygen. The black dotted CV represents the reduction of oxygen in dry acetonitrile with a glassy carbon working electrode with a peak reduction at
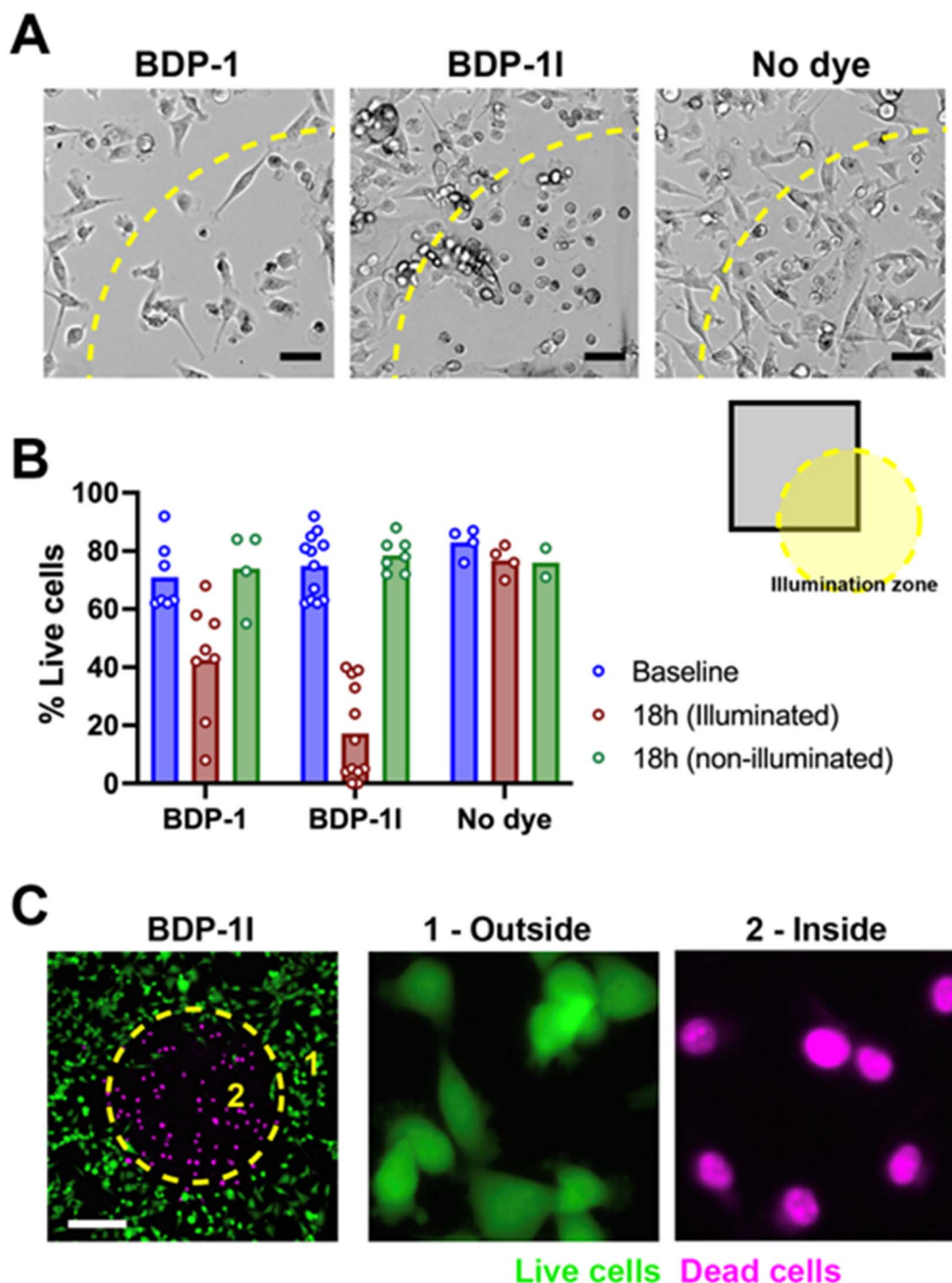

Fig. 6 Photosensitization of breast cancer cells. (A) Bright field images of MDA-MB-231 cells incubated with **BDP-1** or **BDP-1I** and illuminated with low-energy light. Unstained cells (no dye) and non-illuminated regions were used as controls. (B) Quantification of cell viability. Each dot in the graph represents a field of view from two independent biological replicates. Baseline, pre-illumination. (C) Viability of cells incubated with **BDP-1I** assessed with the LIVE/DEAD assay. The dotted circles indicate the illumination zone. Scale bars, 50 μm.

−1.02 V *vs.* Ag/AgCl. Under anaerobic conditions two distinct reduction waves with $E_{pc} = -0.69$ V and -0.94 V for **BDP-1** and $E_{pc} = -0.63$ V and -1.01 V for **BDP-1I**, red CV Fig. 4A and B respectively. Solutions of **BDP-1** and **BDP-1I** saturated with air, blue CV Fig. 4A and B respectively, show an intense reduction wave with $E_{pc} = -0.88$ V *vs.* Ag/AgCl. Presumably, this new redox wave represents reduction of oxygen to superoxide. The 14 mV anodic shift associated with the reduction of oxygen in the presence of the BDP-dyes indicates a strong overlap of the LUMO orbitals, which should facilitate the photo-injection of an electron from these orbitals into molecular oxygen. While these studies show, **BDP-1I** is significantly more efficient than **BDP-1** at generating ROS it seems clear that both dyes work by both a Type I and Type II mechanism.

3.3. Cell studies

We tested ER localization of **BDP-1** by immunostaining cells for the Lys–Asp–Glu–Leu (KDEL) peptide, characteristic of ER-resident proteins (Fig. 5A). **BDP-1** signals formed a meshwork of vesicular patterns typical of the ER, with KDEL localized within this meshwork. These results also show that **BDP-1** fluorescence is preserved in cells after fixation. **BDP-1** fluorescent patterns also overlapped with those from the ER-Tracker dye (Fig. 5B, top) and were retained for at least 24 h in live cells (ESI, Fig. S10†). **BPD-1I** localization was similar to that of **BDP-1**, but the iodinated PS produced lower intensity signals, as expected (Fig. 5B, bottom). In contrast, **BDP-1** signals poorly overlapped with fluorescence from MitoTracker, a mitochondrial-specific dye (Fig. 5C). Although we do not exclude some localization of **BDP-1** and **BDP-1I** to intracellular vesicles, the results confirm that the PSs primarily localize to the ER.

BDP-1 and **BDP-1I** photosensitizing abilities were evaluated using an aggressive breast cancer cell line (MDA-MB-231). There was no cytotoxicity of the BDP dyes in the absence of illumination (Fig. 6). MDA-MB-231 cells pre-incubated with **BDP-1**, **BDP-1I,** or in the absence of dye were irradiated using the 'Cy3' illumination setting of the microscope LED system, focalizing the light beam on a defined region of the culture. Bright field images taken 40 h after the PDT treatment showed a clear PS effect for **BDP-1I** and a more modest effect for **BDP-1** in illuminated regions (Fig. 6A and B). Cytototoxicity of the **BDP-1I** + light combination was confirmed using viability staining (Fig. 6C).

The 'Cy3' illumination setting, while convenient to visualize the BDP dye, does not fully cover the absorption spectra of **BDP-**
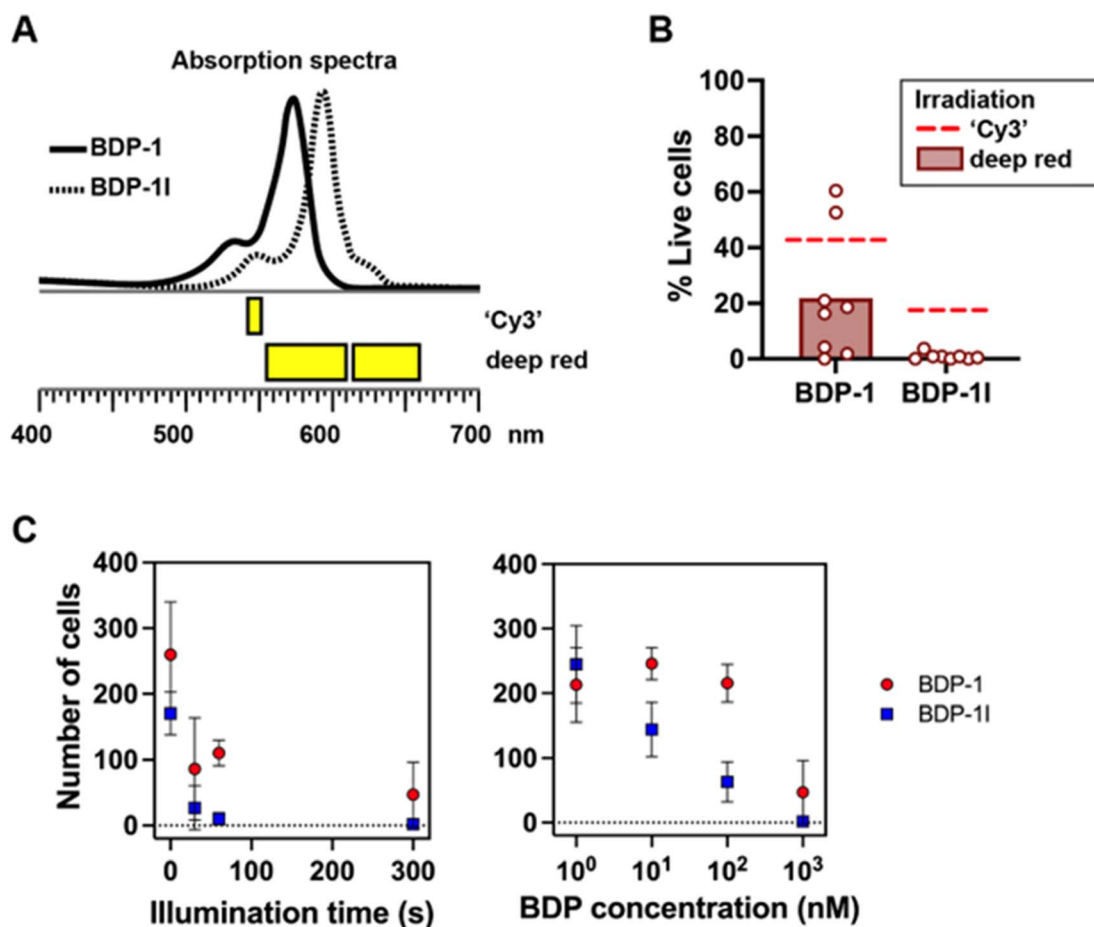

Fig. 7 Photosensitization of cancer cells. (A) Irradiation wavelengths with 'Cy3' excitation (as used for Fig. 5) and by combining 575 and 630 nm LEDs (deep red). (B) Viability of MDA–MD–231 breast cancer cells incubated with **BDP-1** or **BDP-1I**, after irradiation with deep red light. Dashed lines show average viability values after 'Cy3' irradiation for comparison (Fig. 5B). (C) Number of live cells within the illumination zone as a function of the duration of the irradiation (left) and the concentration of the BDP photosensitizers (right).

1 and **BDP-1I** (Fig. 7A), which may lead to an underestimation of their PS action. We therefore repeated measurements of cancer cell viability, using irradiation wavelengths better overlapping the **BDP-1** and **BDP-1I** absorption spectra (Fig. 7A and B). The results confirm that **BDP-1I** is more potent than **BDP-1** at killing cancer cells. They also show that using a broader range of wavelengths increases the cytotoxic effects of **BDP-1** and **BDP-1I**. For cells pre-incubated with **BDP-1I** and irradiated with the broader deep red wavelengths, survival in the irradiation zone was <1% (compared to 17% with 'Cy3' irradiation). The PS effect was dependent on both the length of irradiation and the concentration of **BDP-1** and **BDP-1I** (Fig. 7C).

Phototoxicity of **BDP-1I** was confirmed in a second breast cancer cell line (HMT3522-T4) (ESI Fig. S11†). Here also, cell death observed in bright field was confirmed with cell viability staining. The **BDP-1** and **BDP-1I** treatments combined with light lead to ~20% and ~50% loss of viability, respectively, within 18 h following irradiation. Note that in the BDP treatment conditions, cells were lost in the illumination regions post-illumination, likely due to apoptosis. The apoptotic process is characterized by chromatin marginalization followed by pyknosis (condensation) and Karyorrhexis (fragmentation). These phenotypes are clearly visible in the DAPI stain inside the irradiation zone of cancer cells treated with **BDP-1I** (ESI Fig. S13D†). In contrast, outside the irradiation zone most cell nuclei had normal interphase morphologies, and many mitotic figures were detected. With a loss of dead cells in irradiated regions, the proportion of cell killing by **BDP-1I** may have been underestimated.

Cytotoxicity of **BDP-1I** combined with illumination was also measured in non-cancerous breast epithelial cells (HMT3522-S1) (ESI Fig. S12†). It was therefore not limited to cancer cells, as expected. Toxicity of the PS was strictly restricted to the illuminated zones. In this cell line, the combined cytotoxic effect of **BDP-1** and illumination was minimal.

4. Conclusions

Here in we describe a simple two-step synthetic route toward two BDP dyes with the ability to localize within the ER of normal and cancerous breast cells without the need for complex post-functionalization. These BDP dyes showed the ability to generate ROS by both the Type I and Type II mechanism albeit **BDP-1I** shows considerably greater ROS production. As designed, **BDP-1I** demonstrated the ability to act as a PDT agent with significant killing of two different breast cancer cell lines. On the other hand, **BDP-1** showed a modest ability to generate ROS upon illumination *in vitro*; however, it demonstrated a considerable ability to kill breast cancer cells.

While our target BDP dye, **BDP-1I**, behaved as an ER-localizing PDT agent, as designed, inclusion of its congener, **BDP-1**, was primarily for comparison, to illustrate the advantages of the *ortho*-iodophenyl substituent in generating ROS. *In vitro* ROS studies proved our hypothesis with **BDP-1** generating limited ROS. However, its ability to show significant cell killing in two different breast cancer cell lines was unexpected. Of greater significance was the observation that irradiated non-

neoplastic breast epithelial cells in the presence of **BDP-1** showed very limited phototoxicity. We believe this unprecedented selective behavior displayed by **BDP-1** suggests that malignant and non-malignant breast cells respond differently to low levels of ROS production within the ER. Further studies are currently underway to gain a better understanding of this result.

Data availability

All relevant data generated and analysed during this study, which include experimental, spectroscopic, and cellular studies, are included in this article and its ESI.†

Conflicts of interest

The authors declare no conflicts of interest.

Notes and references

1 D. E. Dolmans, D. Fukumura and R. K. Jain, *Nat. Rev. Cancer*, 2003, **3**, 380–387.

2 S. B. Brown, E. A. Brown and I. Walker, *Lancet Oncol.*, 2004, **5**, 497–508.

3 R. Bonnett and M. C. Berenbaum, *Adv. Exp. Med. Biol.*, 1983, **160**, 241–250.

4 D. Kessel, *Photochem. Photobiol.*, 1986, **44**, 193–196.

5 P. Cramers, M. Ruevekamp, H. Oppelaar, O. Dalesio, P. Baas and F. A. Stewart, *Br. J. Cancer*, 2003, **88**, 283–290.

6 M. H. Teiten, L. Bezdetnaya, P. Morliere, R. Santus and F. Guillemin, *Br. J. Cancer*, 2003, **88**, 146–152.

7 M. Schroder and R. J. Kaufman, *Mutat. Res.*, 2005, **569**, 29–63.

8 A. S. Lee and L. M. Hendershot, *Cancer Biol. Ther.*, 2006, **7**, 721–722.

9 Y. Zhoua, Z. Liua, G. Qiao, B. Tanga and P. Li, *Chin. Chem. Lett.*, 2021, **32**, 3641–3645.

10 G. P. Collett, C. W. Redman, I. L. Sargent and M. Vatish, *Oncotarget*, 2018, **9**, 6707–6717.

11 A. Ajoolabady, C. Lebeaupin, N. N. Randal, J. Kaufman and J. Ren, *Med. Res. Rev.*, 2022, **43**, 5–30.

12 X. Lou, D. Gao, L. Yang, Y. Wang and Y. Hou, *J. Transl. Med.*, 2023, **21**, 1–13.

13 H. Yoshida, *FEBS J.*, 2007, **274**, 630.

14 K. Xue, P. Wei, W. Qi, L. Jia, L. Tong and Z. Qi, *Dyes Pigm.*, 2023, **219**, 111652.

15 X. Li, N. Kwon, T. Guo, Z. Liu and J. Yoon, *Angew. Chem., Int. Ed.*, 2018, **57**, 11522–11531.

16 Y. He, J. Shin, W. Gong, P. Das, J. Qu, Z. Yang, W. Liu, C. Kang, J. Qu and J. Kim, *Chem. Commun.*, 2019, **55**, 2453–2456.

17 H. Lee, Z. Yang, Y. Wi, T. W. Kim, P. Verwilst, Y. H. Lee, G. Han, C. Kang and J. Kim, *Bioconjugate Chem.*, 2015, **26**, 2474–2480.

18 F. Jong, J. Pokorny, B. Manshian, B. Daelemans, J. Vandaele, J. B. Startek, S. Soenen, M. Van der Auweraer, W. Dehaen, S. Rocha and G. Silveira-Dorta, *Dyes Pigm.*, 2020, **176**, 108200.

19 D. Singh, D. Rajput and S. Kanvah, *Chem. Commun.*, 2022, **58**, 2413–2429.

20 A. Fujisawa, T. Tamura, Y. Yasueda, K. Kuwata and I. Hamachi, *J. Am. Chem. Soc.*, 2018, **140**, 17060–17070.

21 A. Hambrock, C. Loffler-Walz and U. Quast, *Br. J. Pharmacol.*, 2002, **136**, 995–1004.

22 T. Yogo, Y. Urano, Y. Ishitsuka, F. Maniwa and T. Nagano, *J. Am. Chem. Soc.*, 2005, **127**, 12162–12163.

23 A. Turksoy, D. Yildiz and E. U. Akkaya, *Coord. Chem. Rev.*, 2019, **379**, 47–64.

24 A. Kamkaew, S. H. Lim, H. B. Lee, L. V. Kiew, L. Y. Chung and K. Burgess, *Chem. Soc. Rev.*, 2013, **42**, 77–88.

25 I. W. Badon, J.-P. Jee, T. P. Vales, C. Kim, S. Lee, J. Yang, S. K. Yang and H.-J. Kim, *Pharmaceutics*, 2023, **15**, 1512–1527.

26 J. Zou, Z. Yin, K. Ding, Q. Tang, J. Li, W. Si, J. Shao, Q. Zhang, W. Huang and X. Dong, *ACS Appl. Mater. Interfaces*, 2017, **9**, 32475–32481.

27 D. Wang, N. S. D. Solomon, I. Pernik, B. A. Messerle and S. T. Keaveny, *Aust. J. Chem.*, 2020, **73**, 979–986.

28 M. Ucuncu, E. Karakus, E. K. Demirci, M. Sayar, S. Dartar and M. Emrullahoglu, *Org. Lett.*, 2017, **19**, 2522–2525.

29 J. Sun, F. Zhong, X. Yi and J. Zhao, *Inorg. Chem.*, 2013, **52**, 6299–6310.

30 W. Wu, J. Sun, X. Cui and J. Zhao, *J. Mater. Chem. C*, 2013, **1**, 4577–4589.

31 E. R. H. Walter, R. K.-K. Leung, L. C.-C. Lee, K. K.-K. Lo and N. J. Long, *J. Mater. Chem. B*, 2024, **12**, 10409.

32 Z. Kang, W. Bu, X. Guo, L. Wang, Q. Wu, J. Cao, H. Wang, C. Yu, J. Gao, E. Hao and L. Jiao, *Inorg. Chem.*, 2024, **63**, 3402–3410.

33 S. Swavey, D. Heidary, E. Boyd and J. Erb, *Eur. J. Org Chem.*, 2023, e202300777.

34 T. Yogo, Y. Urano, Y. Ishitsuka, F. Maniwa and T. Nagano, *J. Am. Chem. Soc.*, 2005, **127**, 12162–12163.

35 E. Bassan, Y. Dai, D. Fazzi, A. Gualandi, P. G. Cozzi, F. Negri and P. Ceroni, *Photochem. Photobiol. Sci.*, 2022, **21**, 777–786.

36 T. D. Lash and B. Gandhi, *J. Org. Chem.*, 2000, **65**, 8020–8026.

37 M. Ucuncu, E. Karakus, E. K. Demirci, M. Sayar, S. Dartar and M. Emrullahoglu, *Org. Lett.*, 2017, **65**, 8020–8026.

38 A. P. Thomas, P. S. S. Babu, S. A. Nair, S. Ramakrishnan, D. Ramaiah, T. K. Chandrashekar, A. Srinivasan and M. R. Pilai, *J. Med. Chem.*, 2012, **55**, 5110–5120.

39 Y. Gao, X. Wang, X. He, Z. He, X. Yang, S. Tian, F. Meng, D. Ding, L. Luo and B. Z. Tang, *Adv. Funct. Mater.*, 2019, **29**, 1902673.

40 T. Ohyashiki, M. Nunomura and T. Katoh, *Biochim. Biophys. Acta, Rev. Biomembr.*, 1999, **I421**, 131–139.

41 F. Wilkinson, W. Phillip and A. B. Ross, *J. Phys. Chem.*, 1993, **22**, 113–218.

42 M. Garcia-Diaz, Y.-Y. Huang and M. R. Hamblin, *Methods*, 2016, **109**, 158–166.

43 T. Entrada, S. Waldron and M. Volk, *J. Photochem. Photobiol., B*, 2020, **204**, 111787.

44 Y. Gao, X. Wang, X. He, X. Yang, S. Tian, F. Meng, D. Ding, L. Luo and B. Z. Tang, *Adv. Funct. Mater.*, 2019, **29**, 1902673.

45 H. Zhao, X. Kalivendi, H. Zhang, J. Joseph, K. Nithipatikom, J. V. Vivar and B. Kalyanaraman, *Free Radical Biol. Med.*, 2003, **34**, 1359–1368.

46 K.-X. Teng, W.-K. Chen, L.-Y. Niu, W.-H. Fang, G. Cui and Q. Z. Yang, *Angew. Chem., Int. Ed.*, 2021, **60**, 19912–19920.

47 Z. Zhuang, J. Dai, M. Yu, J. Li, P. Shen, R. Hu, X. Lou, Z. Zhao and B. Z. Tang, *Chem. Sci.*, 2020, **11**, 3405–3417.

48 H. Huang, S. Banerjee, K. Qiu, P. Zhang, O. Blacque, T. Malcomson, M. J. Paterson, G. J. Clarkson, M. Staniforth, V. G. Stavros, G. Gasser, H. Chao and P. J. Sadler, *Nat. Chem.*, 2019, **11**, 1041–1048.

49 J. Davila and A. Harriman, *Photochem. Photobiol.*, 1989, **50**, 29–35.